RSC Advances

PAPER

View Article Online
View Journal | View Issue

Cite this: *RSC Adv.*, 2021, **11**, 6667

Promoting dry reforming of methane *via* bifunctional NiO/dolomite catalysts for production of hydrogen-rich syngas

Mohd Razali Shamsuddin,[a] Nurul Asikin-Mijan,[b] Tengku Sharifah Marliza,[c] Manabu Miyamoto,[d] Shigeyuki Uemiya,[d] Mohd Ambar Yarmo[b] and Yun Hin Taufiq-Yap *[ae]

Extensive effort has been focused on the advancement of an efficient catalyst for CO_2 reforming of CH_4 to achieve optimum catalytic activity together with cost-effectiveness and high resistance to catalyst deactivation. In this study, for the first time, a new catalytic support/catalyst system of bifunctional NiO/dolomite has been synthesized by a wet impregnation method using low-cost materials, and it shows unique performance in terms of amphoteric sites and self-reduction properties. The catalysts were loaded into a continuous micro-reactor equipped with an online GC-TCD system. The reaction was carried out with a gas mixture consisting of CH_4 and CO_2 in the ratio of 1 : 1 flowing 30 ml min^{-1} at 800 °C for 10 h. The physicochemical properties of the synthesized catalysts were determined by various methods including X-ray diffraction (XRD), N_2 adsorption–desorption, H_2 temperature-programmed reduction (H_2-TPR), temperature-programmed desorption of CO_2 (TPD-CO_2), and temperature-programmed desorption of NH_3 (TPD-NH_3). The highest catalytic performance of the DRM reaction was shown by the 10% NiO/dolomite catalyst (CH_4 & CO_2 conversion, χCH_4; $\chi CO_2 \sim 98\%$ and H_2 selectivity, $S_{H_2} = 75\%$; $H_2/CO \sim 1:1$ respectively). Bifunctional properties of amphoteric sites on the catalyst and self-reduction behaviour of the NiO/dolomite catalyst improved dry reforming of the CH_4 process by enhancing CH_4 and CO_2 conversion without involving a catalyst reduction step, and the catalyst was constantly active for more than 10 h.

Received 30th October 2020
Accepted 22nd December 2020

DOI: 10.1039/d0ra09246k

rsc.li/rsc-advances

1 Introduction

An International Panel on Climate Change (2014)[1] predicted that the world energy demand for natural gas, oil, and other energy sources will increase extensively. The estimation of worldwide energy utilization, which is associated with rising population and economic growth, was projected to be >40% by the year 2035. Currently, world energy demand is laid on fossil hydrocarbon-coal, petroleum, and natural gas. However, the limited sources and the long-term trend in feedstock prices encourage people to increase the economical use of renewable resources, such as utilizing synthetic gas or syngas.

Syngas is a fuel gas mixture primarily comprised of hydrogen, carbon monoxide and frequently carbon dioxide. It is an essential intermediate for ammonia, methanol, and synthetic hydrocarbon fuel production. The formation of syngas requires high temperatures due to the strongly endothermic reaction. The production of syngas commonly involves a reforming process which includes steam reforming,[2] gasification[3] or partial oxidation of CH_4,[4] and dry reforming CH_4 (DRM).[5]

DRM was introduced by Fischer and Tropsch in 1928 by a catalytic reaction using Ni and Co as the catalysts.[5] This process has advantages for the environment compared to the universally admitted harmful effect of CO_2. Contrarily, DRM is deliberately the most convenient alternative because of the significant output of a higher H_2/CO ratio.[6] Concurrently in the process, CH_4 reacts with an equimolar amount of CO_2 over a catalyst to produce H_2 and CO (1). Nevertheless, because of the high temperature (650–1000 °C) which is required for the reaction, active catalyst material sintering and coke formation might occur *via* the eqn (2) and (3).[7–10]

[a]*Catalysis Science and Technology Research Centre (PutraCAT), Chemistry Department, Faculty of Science, Universiti Putra Malaysia, 43400 UPM Serdang, Selangor, Malaysia. E-mail: taufiq@upm.edu.my; Fax: +60 3 89466758; Tel: +60 3 89466809*

[b]*Department of Chemical Science, Faculty of Science and Technology, Universiti Kebangsaan Malaysia, 43650 UKM Bangi, Selangor, Malaysia*

[c]*Department of Basic Science and Engineering, Faculty of Agriculture and Food Sciences, Universiti Putra Malaysia, Bintulu Sarawak Campus, 97008 Bintulu, Sarawak, Malaysia*

[d]*Department of Chemistry and Biomolecular Science, Faculty of Engineering, Gifu University, Japan*

[e]*Faculty of Science and Natural Resources, Universiti Malaysia Sabah, Jln UMS, 88400 Kota Kinabalu, Sabah, Malaysia*

$$CH_4 + CO_2 \rightleftharpoons 2H_2 + 2CO,\ \Delta H^\circ = +247.3\ \text{kJ mol}^{-1},\ \Delta G = 61.770\text{–}67.32T\ \text{kJ mol}^{-1},\ \text{at } T = 643\ ^\circ\text{C},\ \Delta G^\circ = +104.88\ \text{kJ mol}^{-1},\ \text{at } T = 647\ ^\circ\text{C},\ \Delta G^\circ = -164.4\ \text{kJ mol}^{-1} \quad (1)$$

$$CH_4 \rightleftharpoons C + 2H_2,\ \Delta H^\circ = +75\ \text{kJ mol}^{-1},\ \Delta G = 21.90\text{–}26.45T\ \text{kJ mol}^{-1} \quad (2)$$

$$2CO \rightleftharpoons C + CO_2,\ \Delta H^\circ = -171\ \text{kJ mol}^{-1},\ \Delta G = -39.810 + 40.87T\ \text{kJ mol}^{-1} \quad (3)$$

The major dispute is that it prevents the extensive applications of DRM withstand in catalyst performance. From an economic standpoint, Ni-based catalysts are more appealing than noble metals which are very expensive and often unavailable.[10,55] However, in terms of industrial applications, Ni catalysts are limited due to their unstable performance which is induced by sintering of active Ni species and coke formation on the metal surfaces.[11–13] Therefore, coke deposition presents a major barrier for the DRM reaction over Ni-based catalysts.

To overcome the problem, there are some efficient alternatives to prevent coke deposition, such as (i) doping with alkali/alkaline earth or transition metal promoters, (ii) poisoning of coke-formation sites by sulphur, (iii) dispersing Ni chemically or physically into other metal oxides; (iv) restricting Ni particles in mesoporous materials, (v) and encapsulating Ni particles in an inorganic frame or shell.[10] Utilization of a basic metal such as Mg[14–16] and Ca[17,18] is able to solve this problem by hindering coking mechanisms. Hence, employing dolomite, which contains Mg and Ca, may be a better choice for producing a supreme bifunctional catalyst for the DRM reaction. Noteworthy, the synergetic effect between NiO and dolomite have been proven to hinder coke formation. Although NiO supported on dolomite (NiO/dolomite) was reported to have outstanding catalytic performance in a variety of reaction process such as oil cracking,[19] pyrolysis/reforming,[20] steam reforming,[21] and gasification.[22] However, there is no evidence in the previous literature of NiO/dolomite being used as a catalyst in the DRM reaction.

Due to aforementioned finding, the focus of this study was the use of bifunctional Ni/dolomite catalyst for production of syngas especially H_2 *via* DRM reaction with zero waste production from catalyst synthesis until end of reaction. It is expected that incorporation of Ni and dolomite would form a bifunctional catalyst with strong metal-support interaction, which in thus result in a excellent synergetic effect between both metals and the support. It is believed that this trait will able to enhance the DRM activity and stability of the catalyst.

2 Experimental

2.1 Material

The chemicals involved in the synthesis of the catalyst were $Ni(NO_3)_2 \cdot 6H_2O$ and natural dolomite. Dolomite from Perlis Dolomite Sdn. Bhd. went through a pre-treatment by calcination at 900 °C (Table 1). Dolomite are apparently dominated by Ca (55.6%) and Mg (12.9%) followed by Fe (0.2%) Si (0.1)% and Al (0.1%). $Ni(NO_3)_2 \cdot 6H_2O$ (ACROS, purity 99.8%) was used as received without any pre-treatment.

Table 1 XRF analysis of dolomite composition

Element	*Z*	Concentration[a]
Ca	20	55.56%
Mg	12	12.92%
Fe	26	0.17%
Si	14	0.13%
Al	13	0.11%
Cl	17	0.02%
S	16	0.02%
Sr	38	0.02%
Mn	25	92 ppm
Cu	29	67 ppm
Mo	42	57 ppm
Zr	40	11 ppm

[a] Result obtained from XRF Analysis. Dolomites contain C and O which cannot be detected by XRF spectroscopy which effect to total elemental content is not 100%.

2.2 Catalyst preparation

Five grams of catalyst was prepared by using a wet-impregnation method. 10 w/w% of $Ni(NO_3)_2 \cdot 6H_2O$ was dissolved in distilled water and stirred for one hour. Dolomite was added, and the mixture was continuously heated at 100 °C until all of the water evaporated. The sludge-like catalyst was then oven-dried at 150 °C for 24 h. Then, the dried catalyst was ground using mortar and pestle until it became a fine powder before being calcined in a tube furnace heated at 10 °C min^{-1} to 600 °C for 3 h under air atmosphere.

2.3 Physicochemical properties analysis

The physicochemical properties of the prepared catalyst were characterized by X-ray diffraction (XRD), surface area and porosity (BET), Field Emission Scanning Electron Microscopy (FESEM), H_2 temperature-programmed reduction (TPR-H_2), and temperature programmed desorption of CO_2 (TPD-CO_2) and NH_3 (TPD-NH_3). The XRD analysis was determined using a Shimadzu diffractometer model XRD-6000 with Cu-Kα radiation = 1.5418 Å radiation at 2θ between 20° to 80° and a scan speed of 4° min^{-1} to identify the crystal phase of the obtained catalyst.

Nitrogen isotherm adsorption–desorption analysis gave the specific surface area, average pore size, and pore volume distribution of the catalysts. The determination was carried out by using a Micromeritic ASAP2020 instrument at −196 °C. Before the evaluation, the catalyst was degassed at 150 °C for 8 h to take off the water or other adsorbed gases from the catalyst surface. The specific surface area (V_m) was calculated using the BET method at a pressure range of $0.05 < p/p^\circ < 0.30$.

Field Emission Scanning Electron Microscopy (FESEM) images were obtained on a Microscope-Hitachi (FESEM-Hitachi model) at high magnification combined with Energy Dispersive X-ray analysis (EDX) for quantitative determination of the amount of metal loading.

The ground catalysts were placed evenly on top of an aluminium stub with double-sided carbon tape and coated with platinum before testing in order to avoid electrical charging during catalyst analysis.

Temperature programmed reduction (TPR-H_2) and temperature-programmed desorption (TPD-CO_2 & TPD-NH_3) analysis were performed using the Thermo Finnigan TPD/R/O 1100 Instrument. About 0.05 g of the catalysts were inserted into a quartz tube reactor with an internal diameter of 6 mm, and then they were pre-treated under 20 ml min^{-1} N_2 gas flow at 150 °C for 10 min. The analysis condition was carried out using 5% H_2/Ar flow at 25 ml min^{-1} from 50 to 900 °C with a heating ramp of 10 °C min^{-1}. Hence, to prove the *in situ* reduction of NiO/dolomite catalyst under CH_4 reductant, the reaction model was conducted using a Micromeritics Autochem II+ Enhanced Chemisorption Analyzer connected with mass spectrometer model Cirrus 2 Quadrupole. The transient MS signals at a mass-to-charge ratio (m/z) of 2, 16, 18, 28, and 44 were measured continuously for H_2, CH_4, H_2O, CO, and CO_2, respectively. For TPD-CO_2 and TPD-NH_3, the pre-treatment was performed under a N_2 flow of 20 ml min^{-1} at 300 °C for 30 min. Then the catalyst was exposed to CO_2 and NH_3 gas (30 ml min^{-1}) at ambient temperature for 60 min and cleaned by N_2 flow for 30 min to remove the excess CO_2 or NH_3 on the catalyst surface. The analysis was conducted using helium gas with 25 ml min^{-1} flow from 60 to 900 °C with a heating ramp of 10 °C min^{-1}. All analysis were identified by a thermal conductivity detector (TCD).

2.4 Catalytic performance

The model biogas reforming (DRMC) reaction was conducted using a fixed bed stainless steel micro-reactor with internal diameter, $Ø = 6$ mm, and height, $h = 340$ mm, in the continuous flow system. In a prior reaction for some catalysts, ~0.20 g catalyst was reduced in 5% H_2/Ar at a flow rate of 30 ml min^{-1} and temperatures from 100 to 700 °C for 1 h in order to determine the effect of the reduction environment on catalytic activity. The DRM reaction was performed using a mixture of gases consisting of CH_4 and CO_2 with molar ratio 1 : 1 without dilution. The measurement was carried out by flowing the feed gas (30 ml min^{-1}) at 1 atm and 800 °C and holding for 600 min. The gas products were analysed by an online gas chromatograph with a TCD detector, Agilent 6890N (G 1540N) equipped with Varian capillary columns "HPPLOT/Q and HP-MOLSIV". Fig. 1 shows the schematic diagram of the catalytic micro-reactor system.

2.5 Carbon formation on spent catalyst analysis

To evaluate the deposited carbon during the DRM reaction, the images and amount of carbon accumulated after 10 h of the reaction were analysed. A comparative study of fresh and spent catalysts to determine carbon formation was carried out on an FESEM model JEOL JSM7600F at 20 K magnification and a transmission electron microscope (LEO 912AB).

Determination of crystal phases that appeared after the DRM reaction was conducted using XRD analysis (Shimadzu XRD-6000). Quantitative analysis of carbon formation was performed in a Mettler-Toledo TGA/DSC1 instrument. The coked catalyst was submitted to a heat treatment under 5% O_2/N_2 (100 cm^3 min^{-1}) with a heating rate of 10 °C min^{-1}. Thus, the amount of carbon burned out was determined by the weight loss of CO_2 and CO produced during the analysis.

3 Results and discussion

3.1 X-ray diffraction spectroscopy (XRD)

The XRD profiles of dolomite and NiO/dolomite based catalysts are shown in Fig. 2. The raw dolomite (dolomite$_{raw}$) and

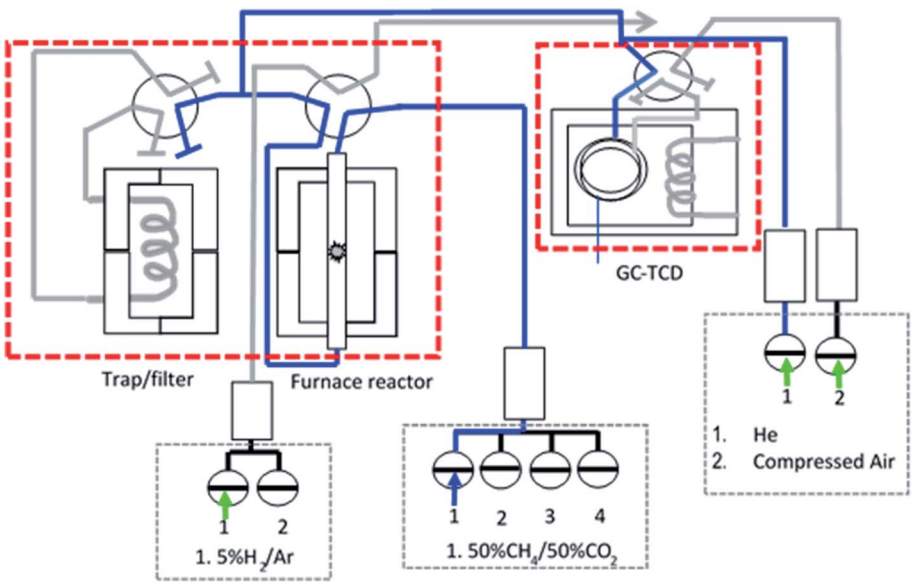

Fig. 1 Schematic diagram of fixed bed stainless steel micro-reactor equipped with online TCD gas chromatography in a continuous flow system.

dolomite calcined at 900 °C, (dolomite$_{900}$) (Fig. 2a) shows a few changes in the crystallite system during the preparation of the catalyst. The calcination step at 900 °C during the pre-treatment promoted half decomposition of dolomite. However, only some part of the dolomite, ($CaMg(CO_3)_2$) suffered from this half decomposition due to the presence of dolomite peaks (ICDD 00-075-1765) on the XRD profiles. Half decomposition of dolomite creates a new crystal phase in a mixture of $CaCO_3$ and $Mg(OH)_2$ which was confirmed by the appearance of peaks $CaCO_3$ (ICDD 00-001-0837) at planes $2\theta =$ 29.36° (014), 39.49° (113), 43.25° (202), 47.30° (024), 57.56° (122), 61.34° (119) and 76.89° (220). Meanwhile, for hexagonal $Mg(OH)_2$ (JCPDS no. 01-1169) plane $2\theta = 18.66°$ (001), 50.98° (102), 62.26° (103) proves the existence of this crystal phase in the catalyst. Formation of $Mg(OH)_2$ is due to the interaction of MgO with moisture at room temperature during sample storage. Decomposition of dolomite involved three different paths: one step/full decomposition[23,24] and two-step/half decomposition[25–27] routes and formation of a "mixed crystal" between calcite and magnesite.[28] Chemical eqn (4)–(7) show the decomposition steps that occurred in the dolomite system.

One step/full decomposition:

$$CaMg(CO_3)_2 \rightarrow CaO + MgO + 2CO_2 \quad (4)$$

Two step/half decomposition:

$$\text{(i) } CaMg(CO_3)_2 \rightarrow CaCO_3 + MgO + CO_2 \quad (5)$$

$$\text{(ii) } CaCO_3 \rightarrow CaO + CO_2 \quad (6)$$

Mixed crystal formation:

$$CaMg(CO_3)_2 \rightarrow CaCO_3(1 - n)MgCO_3 + nMgO + nCO_2 \quad (7)$$

Based on the phase that appeared in dolomite$_{900}$, it can be suggested that calcination of dolomite during the pre-treatment step followed eqn (5), which proves that dolomite is a very stable compound.

Investigation of 5–15% NiO/dolomite after calcination (Fig. 2b) at 600 °C for 3 h exposed the presence of a sharp diffraction peak of dolomite, which is nearly identical to a dolomite$_{raw}$ catalyst, located at 2θ between 20° to 78° (ICDD 00-011-0078). The wet impregnation method consequently took place after pre-treatment of dolomite restructured the crystallite form of dolomite. Sibley *et al.* (1987)[29] proved that the dolomization process can occur at 175 °C where calcite, $CaCO_3$, can be transformed to dolomite with an optimum Mg/Ca ratio. These results reveal that there was crystallographic control in the advancement of the reactant-product interface through which CO_2 diffused outside while the reaction progressed from the surface towards the core.[30] Impregnation of NiO in/on dolomite support was proven successful by the appearance of NiO crystal peaks in the XRD pattern at $2\theta = 37°$, 43°, 62°, 75° and 79°, which respectively corresponded to (111), (200), (220), (311) and (222) planes of cubic NiO species (ICDD 00-022-1189). The peaks at 43° and 62° were determined as overlapping peaks for dolomite, NiO and $MgNiO_2$. It was confirmed that Ni and dolomite formed a stable phase of $MgNiO_2$, which increased the degree of Ni distribution and hindered Ni agglomeration in the DRM process.[19]

As proved by Table 2. NiO crystallite size increased as the following order: 5% NiO/dolomite > 15% NiO/dolomite > 10% NiO/dolomite. These crystal size increased from 27 to 77 nm due to agglomeration of the NiO species. 10% NiO/dolomite show finest crystallite size, and this might be due to uniform distribution of NiO particle on dolomite surface. In addition, comparative value of NiO percentages of dispersion and particle sizes shows *vice versa* trend. It has been confirmed that 10% NiO/dolomite show high NiO dispersion compared to 15% Ni loading. Hence, it can be deduced that upon increasing the Ni percentage, these NiO peaks became intensified, while those corresponding to dolomite remain the same, which thereby corroborates greater dispersion and produced fine particle and crystallite size.

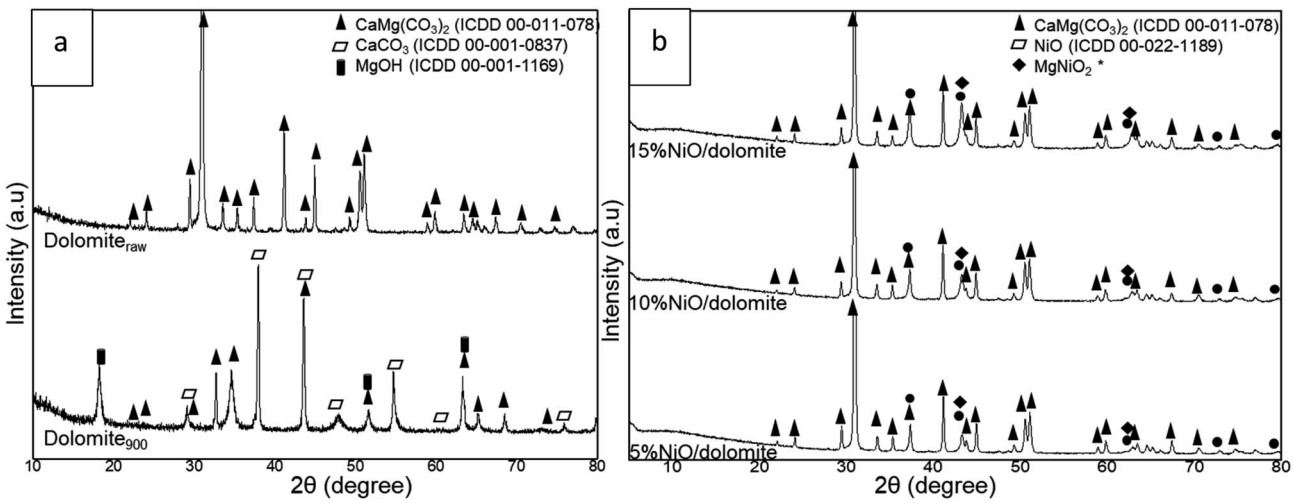

Fig. 2 XRD profile of (a) dolomite$_{raw}$ (raw dolomite) and dolomite$_{900}$ (calcined at 900) and (b) NiO/dolomite catalysts series.

Table 2 Physicochemical properties of catalysts

Analysis	NiO	NiO	Average NiO			TPR-H_2		TPD-CO_2		TPD-NH_3	
Catalysts	Crystallite size (nm)	Dispersions[a] (%)	Particle size[a] (nm)	S_{BET} ($m^2\ g^{-1}$)	Pore size (nm)	Temp. (°C)	Amount (μmol g^{-1})	Temp. (°C)	Amount (μmol g^{-1})	Temp. (°C)	Amount (μmol g^{-1})
Dolomite	—	—	—	17	16.50	807	3950	804	22 488	635	3293
5% Ni/dolomite	33	62.26	23.6	4	11.59	443	557	777	20 948	655	2191
						771	8073				
						827	1977				
10% Ni/dolomite	27	40.55	36.3	25	11.67	401	1407	771	15 357	685	7969
						765	5499				
15% Ni/dolomite	76	19.87	74.1	10	22.27	433	1121	768	17 603	663	3361
						746	2265				

[a] Results obtained from TPDRO analysis.

3.2 Physisorption analysis

Based on Fig. 3a 10% NiO/dolomite displayed a significant Type IIB with H3 hysteresis pattern. This isotherm displays physisorption behaviour for mesoporous which are responsible for the hysteresis and macroporous, with the plateau-like mesoporous.[31,32] The H3 hysteresis pattern expressed plate-like particles for non-rigid aggregates. Hence, the pore network consisted of macropores which were not filled with pore condensate.[33] $Dolomite_{900}$, 5% NiO/dolomite, and 15% NiO/dolomite showed a type III physisorption isotherm with an H3 hysteresis which corresponded to a nonporous or macroporous solid. These materials showed a very low quantity of gas adsorbed compared to 10% NiO/dolomite, and the lower hysteresis indicated the dominant macroporous character of the catalysts.[32]

Fig. 3b shows the BJH pore-size distribution plotted from dV/d (log D) *versus* pore diameter. For all catalysts, the distribution is unimodal with a dominant peak between 10–100 nm. Kuila & Prasad (2013) and Jullien *et al.* (2005)[31,34] summarized that this pore-size distribution can be associated with porosities of '*intra-aggregate*' or large mesopores and fine macropores (diameter 50–100 nm).

The comparison study of $dolomite_{900}$ and prepared NiO/dolomite catalysts in BET specific surface area (S_{BET}) and average pore sizes are tabulated in Table 2. The S_{BET} and total pore volumes follow the order of 5% NiO/dolomite < 15% NiO/dolomite < $dolomite_{900}$ < 10% NiO/dolomite. The higher S_{BET} obtained by 10% NiO/dolomite is due to the existence of fine mesopores and larger mesopores and macropores contributed by additional NiO particles forming on the external surface area of NiO. However, as the nickel loading increased over the optimum value (15% NiO/dolomite), the S_{BET} dropped significantly due to agglomeration of NiO particles and pore blockage on support. Meanwhile, the average pore size of the prepared catalysts has the following order: 5% NiO/dolomite > 10% NiO/dolomite > $dolomite_{900}$ > 15% NiO/dolomite. As shown by Du Plessis (2007), the relationship between average pore size and S_{BET} is found to be an inverse, with a constant specific surface area times the pore diameter product.[35] This explains why 10% NiO/dolomite shows the lowest average pore size, besides 5% NiO/dolomite. Nevertheless, 15% NiO/dolomite shows higher average pore size due to formation of unimodular pore size in this catalyst. 5% NiO/dolomite shows the lowest textural properties (S_{BET} and pore size) due to total pore blockage on the catalyst. As proven by the adsorption–desorption isotherm and pore distribution plot, a lower quantity of adsorbed and low intensity of plot cause the lowest value of S_{BET}, average pore volume and pore size.

3.3 FESEM-EDX analysis

The FESEM image of dolomite (Fig. 4) showed sand-like particles with an average diameter of 50 nm. The distribution of elements C, O, Mg, and Ca reveals $dolomite_{900}$ without noticeable composition changes. 5% NiO/dolomite exhibited the formation of a thin layer sheet crystal on dolomite particles which decreased the surface area and porosity of dolomite. On

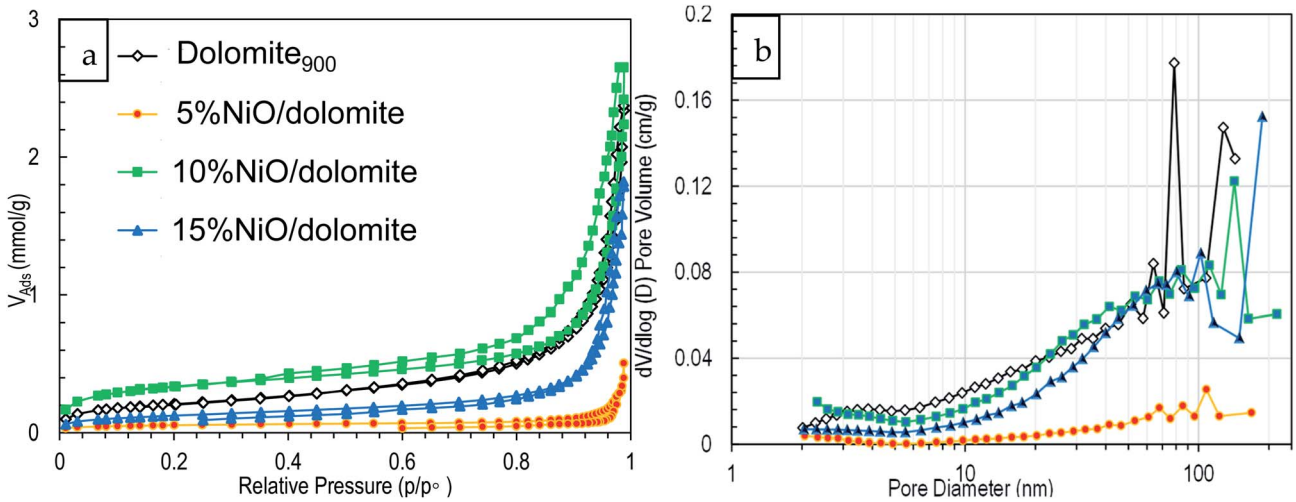

Fig. 3 Physisorption of prepared catalysts series (a) N_2 adsorption–desorption isotherm and (b) pore sized distribution.

the contrary, 10% NiO/dolomite presented aggregate structures. NiO particles were uniformly distributed on/in the dolomite surface by creating a solid solution. Thus, there was no clear difference between NiO and dolomite. This solid solution enhanced the external surface area of NiO/dolomite aggregates. However, at the same time, some large pores on dolomite support were blocked. This resulted in an agreement with the physisorption analysis where the BET surface area increased but

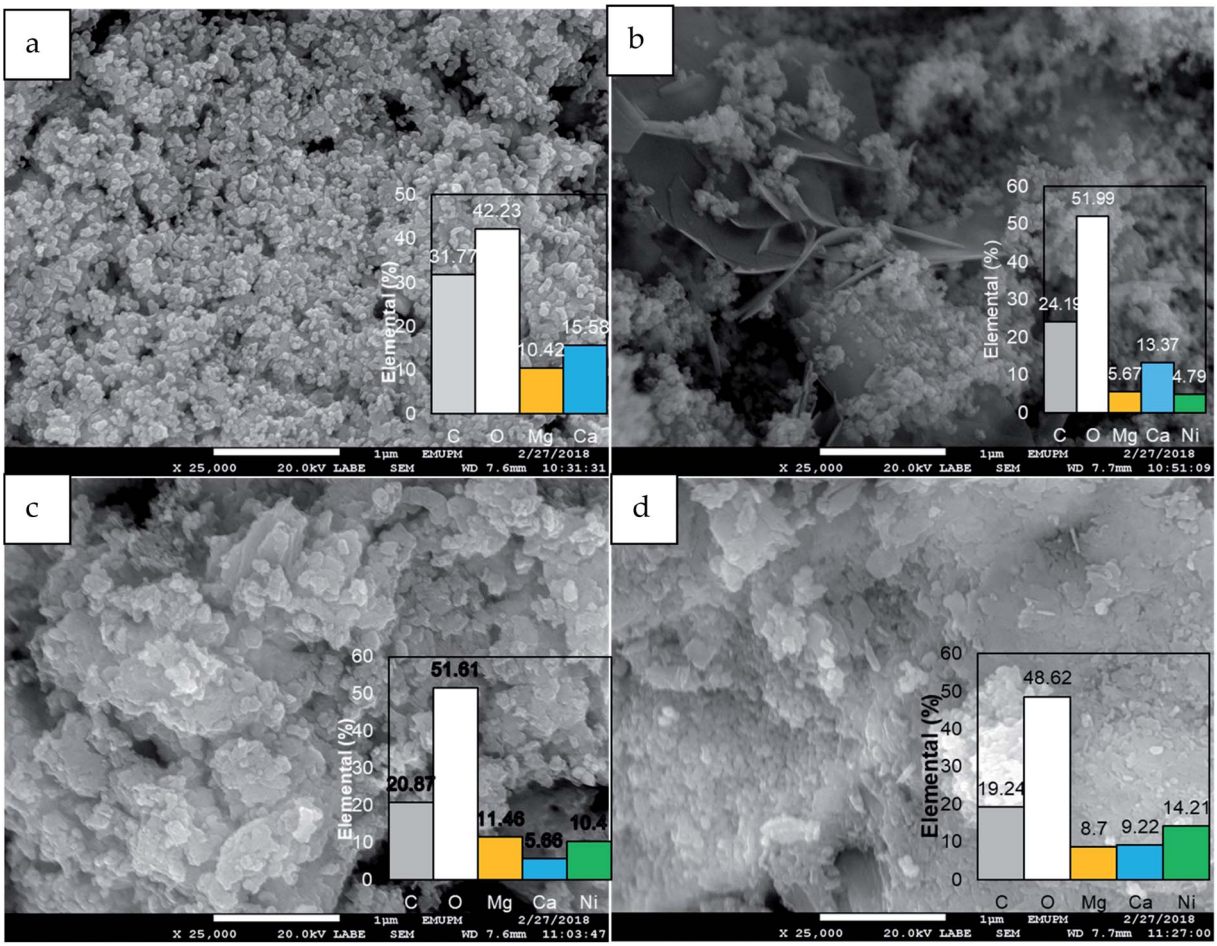

Fig. 4 Field emission scanning microscopy (FESEM) images combined with energy dispersive X-ray (EDX) elemental analysis for prepared catalysts (a) dolomite (b) 5% NiO/dolomite (c) 10% NiO/dolomite (d) 15% NiO/dolomite.

pore size decreased. Excessive addition of NiO (15% NiO/dolomite) tends to form an agglomeration of aggregates which reduces the surface area of dolomite. Nevertheless, these agglomerated particles provide large pores which contribute to the increment of pore size. EDX spectroscopy obtained for a series of catalysts (5%/15% NiO/dolomite) proves that NiO was successfully impregnated into the dolomite support in the desired amount. Also, NiO dispersion (Table 2) proved that as the amount of NiO loading increases from 5% to 15%, the degree of dispersion shows different behaviour on the dolomite support. 10% NiO/dolomite shows the highest degree of Ni dispersion followed 15% NiO/dolomite and 5% NiO/dolomite. This might be due to the interaction between NiO and support. Thus, a low amount of NiO results in low dispersion, but a too high amount also can cause agglomeration of NiO particles and at the same time reduce the dispersion degree.

3.4 Chemisorption analysis

3.4.1 Reduction behaviour. The TPR profiles of dolomite$_{900}$ (Fig. 5a) gave the highest maximum peak at 807 °C, which referred to the existence of CaO/MgO species on the support. Fig. 5b shows XRD profiles of dolomite$_{900}$ and reduced dolomite (Dolomite_R), the results suggest that reduction of dolomite$_{900}$ leads to degradation of the dolomite phase as described by eqn (4)–(7). Degradation of dolomite$_{900}$ produced $Ca(OH)_2$, CaO, and MgO. The appearance of three major peaks on Dolomite_R XRD profiles proves the existence of $Ca(OH)_2$ (ICDD 00-001-1079), CaO (ICDD 01-077-2010), and MgO (00-001-1235) phases. Throughout the reduction, dolomite$_{900}$ (which contains $CaCO_3$) was degraded due to the high temperature and produced CaO and CO_2. Then, CaO reacts with H_2 to produce $Ca(OH)_2$. Meanwhile, $Mg(OH)_2$ reacts with H_2 to simultaneously produce MgO at a higher temperature (around 650–850 °C) in the presence of H_2. Meanwhile, the reduction of NiO/dolomite catalysts shows two dominant peaks at a modest temperature range of 401–443 °C and broad peaks at the higher temperature of 746 827 °C. The first reduction peak can be described as the reduction of Ni^{2+} to Ni^0 on the surface.[36] The XRD diffractogram of reduced catalysts (Fig. 5c) confirmed the formation of Ni^0 species (ICDD 01-087-9414) after NiO/dolomite (5–15%) was reduced by 5% H_2/Ar. Whereas, the broad peak with a shoulder at the higher temperature can be ascribed to Ni reduction with a strong interaction with the support. The $NiMgO_2$ spinel was proven by the XRD diffractogram.[36] In good agreement with this, Ni reduction peaks are presented at around 800 °C with the periclase form of $NiMgO_2$.[37–39] Simultaneously, the degradation of species existing on dolomite$_{900}$ also occurred at this high temperature, which is proven by the presence of extremely broad peaks on the NiO/dolomite catalysts. The degree of NiO reduction for NiO/dolomite was variable due to the addition the different loadings of NiO. It is described by the following order: 5% NiO/dolomite < 10% NiO/dolomite < 15% NiO/dolomite. These marked results might be contributed by the formation of a solid solution of NiO and MgO. It is noteworthy that the reduction behaviour of the NiO catalysts was strongly affected by the presence of the alkaline earth oxide (MgO) in the catalyst.[40]

The process of NiO reduction is considered to be a complex solid–gas reaction influenced by temperature, the concentration of reducing gas, and the presence of additives.[41] Manukyan *et al.* (2015) reported that this reduction starts with initial nucleation of Ni in the temperature range of 543–773 K (270 to

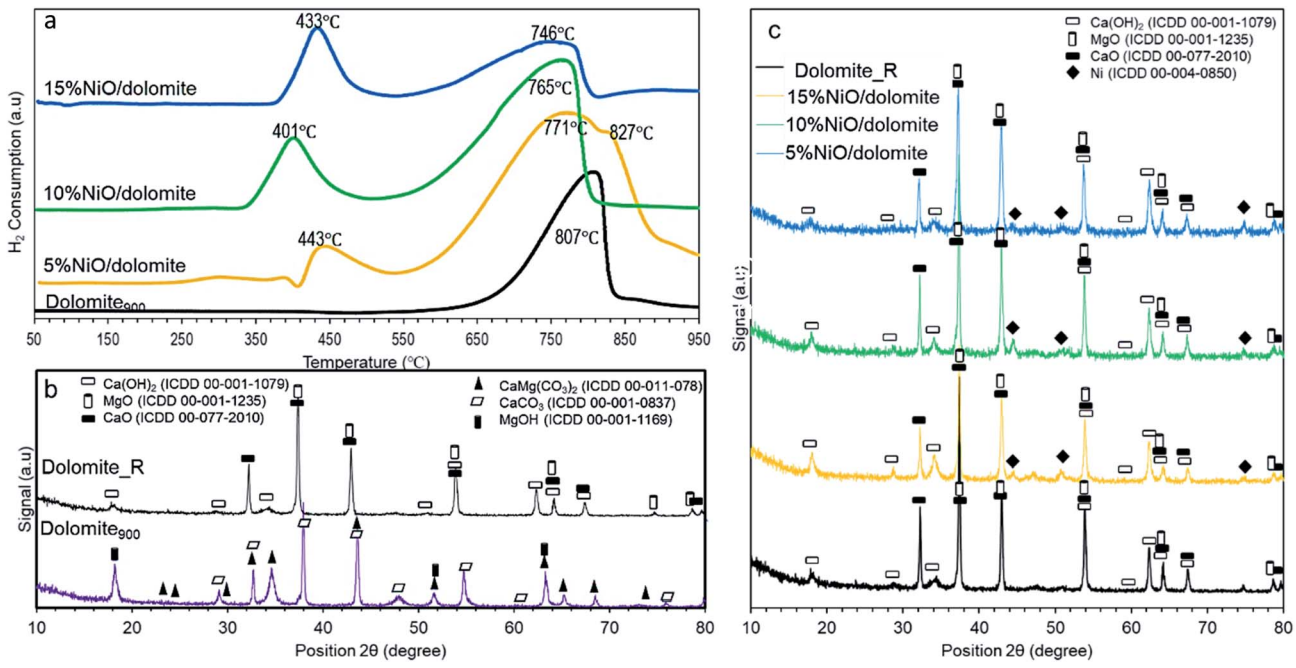

Fig. 5 (a) Temperature-programmed reduction of hydrogen (H_2-TPR) profile from 50 °C to 950 °C (b) XRD profile of dolomite and reduced dolomite (c) XRD profile of reduced catalysts.

500 °C).[42] During this phase, the Ni nuclei emerged on the NiO particles' outer surface. This slow process then underwent the creation of a small channel that commenced to propagate and start the second step of reduction.[42] Consequently, a dominant peak appeared at 550 to 900 °C, referring to the second step of reduction on the bulk of the NiO and $NiMgO_2$ particles. The small channel grew into the NiO bulk. Further Ni nucleation occurred on the inner surface of these channels, leading to the formation of Ni nano-layers. Then these nano-layers start branching and interconnect the network until the NiO phase completely reduces to Ni.[42]

3.4.2 Bifunctional acid-based properties. Based on the results obtained on Fig. 6a NH_3 desorption of all catalysts was detected in the strongly acidic region at a maximum temperature of 633–685 °C. Comparatively, dolomite showed desorption of NH_3 at a peak temperature of T_{max} = 635 °C, due to Lewis-acidic surface centres from $Ca(OH)_2$ (ref. 43) and carboxylic acid (–Ca–COOH). Identification of $Ca(OH)_2$ and (Ca–COOH) species on catalysts that adsorbed NH_3 was confirmed by FTIR spectra (Fig. 6b). This is proved the existence of a hydroxyl group (O–H) and a carboxyl group (C–O) at 3640 cm^{-1} and 1195 cm^{-1} respectively. Dolomite absorbed-NH_3 FTIR shows decreased peak intensity compared to dolomite due to the bonded N–H group on these two functional groups. Hence, NH_3 bonded to $Ca(OH)_2$ and (–Ca–COOH) formed an ammonium ion bonded to oxygen (O^-) on the catalyst as illustrated. Addition of NiO species promotes strong acidic sites in the catalyst system; however, an excess of NiO species rendered diminished acidic sites (Table 2). The strongest and highest acidic sites were detected in 10% NiO/dolomite (T_{max}: 685 °C, 7969 μmol g^{-1}). Meanwhile, the acidic properties of 15% NiO/dolomite decreased monotonously due to agglomeration of Ni particles. These agglomerations reduced Ni surface area, which consequently hindered the active Ni species' ability to adsorb NH_3 molecules. The NH_3 desorption as a function of acidic strength increased according to the following order: dolomite < 5% NiO/dolomite < 15% NiO/dolomite < 10% NiO/dolomite. Analysis of NH_3 absorbed catalysts by FTIR spectra proved the existence of N–H bonding on NiO/dolomite catalysts (5–15%) due to appearance of N–H bending (1430 cm^{-1}) and N–H out-of-plane bending (875 cm^{-1}). 10% NiO/dolomite shows the highest intensity of an N–H bonding group, which means that it has the highest acidity compared to other catalysts. This finding is in agreement with the FESEM images (Fig. 4) and BET specific surface area.

As it is evidenced by Hakim *et al.* 2016,[44] basic properties enhance adsorption of acidic CO_2 molecules more easily on the catalyst surface. Based on the TPD-CO_2 profile (Fig. 6b), the temperature intervals were estimated for very strong sites with the maximum temperature range of 768–804 °C (refer Table 2). Dolomite showed the highest amount of adsorption capacity compared to other catalysts (22 488 μmol g^{-1}), which was contributed by the basic properties of CaO–MgO of alkaline earth metal. FTIR spectra at wavelengths of 1650 cm^{-1} (polydentate), 1440 cm^{-1} (bidentate), and 1130 cm^{-1} (monodentate) indicate asymmetric vibrations of O–C–O, O–CO symmetric vibrations, and C–OH stretching for bicarbonate, respectively.[45] Thus, only bicarbonate has been detected on dolomite without CO_2 adsorption, due to carbonate backbone of dolomite crystal system. 10% NiO/dolomite showed the lowest CO_2 desorption

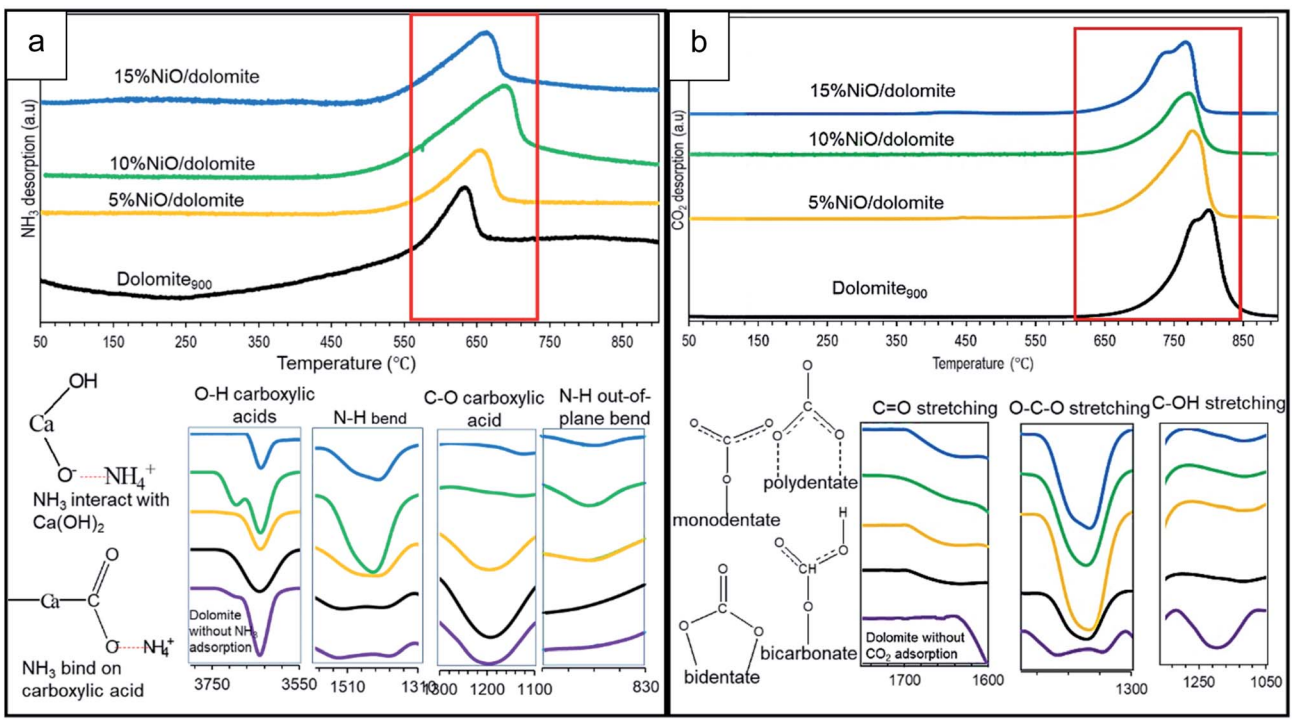

Fig. 6 Bifunctional acid-based properties of (a) temperature programmed desorption of NH_3 combined with FTIR spectrum of NH_3 adsorbed catalysts (b) temperature programmed desorption of CO_2 combined with FTIR spectrum of CO_2 adsorbed catalysts.

temperature among prepared catalysts (T_{max} = 771 °C, 15 357 μmol g^{-1}). The acid strength from NiO decreased basic site densities (nCO_2) of the catalyst. These are caused by the accessibility of CO_2 towards basic sites on dolomite hindered by NiO particles which coincides with decreasing of materials specific surface area (dolomite).[46] However, the amount of CO_2 desorption for 15% NiO/dolomite was a little bit higher than 10% NiO/dolomite, due to the agglomeration of NiO particles which affected its distribution and thus lowered the surface area of the catalyst.

3.5 Catalytic performance

3.5.1 Effect of reduction environment. Fig. 7 shows the results obtained from reduced Ni/dolomite, which was reduced at 700 °C in a 5% H_2/Ar atmosphere for 1 h, and unreduced NiO/dolomite catalysts. Only 10% NiO/dolomite was used to understand how reduction affected the DRM reaction (800 °C for 540 min). Highest CH_4 conversion (99%) was showed by NiO/dolomite catalyst and CO_2 conversions (98%) with the Ni/dolomite catalyst (Fig. 7a). Consequently, NiO/dolomite showed highest H_2 selectivity (~70) compared to Ni/dolomite as the temperature varied (Fig. 7b). The H_2 and CO selectivity of Ni/dolomite was relatively constant (stable) from the beginning of the DRM reaction until 10 h time on stream. This is due to the formation of Ni metal as an active site on the catalyst.

Non-isothermal reduction of NiO/dolomite under a CH_4 environment (CH_4 : N_2 = 1 : 9) was carried out to prove *in situ* reduction of NiO under dry reforming conditions. Fig. 7c demonstrates that the MS signal of CH_4 exhibited this redox reaction only above a temperature of around 250 °C. This was indicated by a significant drop of the signal due to chemical utilization of CH_4 or its adsorption on the NiO surface.

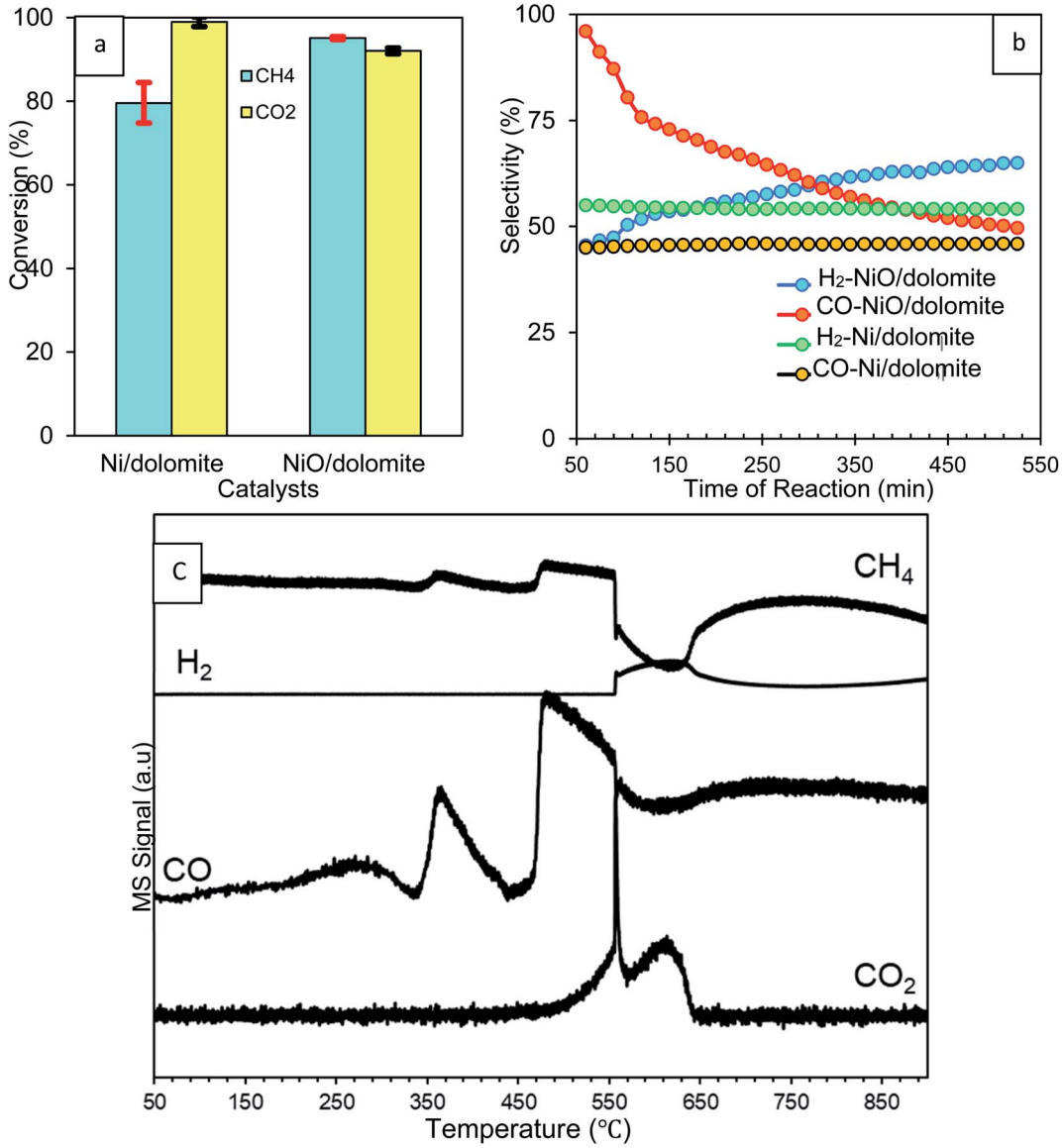

Fig. 7 Effect of reduction step on the percentage of (a) CH_4 and CO_2 conversions (b) H_2 and CO selectivity (c) MS profiles of non-isothermal reduction of 10% NiO/dolomite under CH_4.

Hereafter, CH_4 starts to dissociate to carbon and hydrogen adatoms on NiO as described by the following eqn (8).[47]

$$CH_4 + 5^* \rightarrow C^* + 4H^* \quad (8)$$

$$C^* + NiO \rightarrow Ni^0 + CO + ^* \quad (9)$$

$$2H^* \rightarrow H_2 + 2^* \quad (10)$$

$$CH_4 + \tfrac{1}{2}O_2 \rightarrow CO + 2H_2 \quad (11)$$

Dissociation of CH_4 occurred in two-steps, which first happens on surface and then in the bulk of the catalyst. Consequently, the MS signal of CO peaks detected early at 350 °C are due to the production of carbon adatoms. Ni was produced by the oxidation of these carbon adatoms, and NiO results in the formation of CO (9). H_2 is produced *via* the associative desorption of two hydrogen adatoms (10), and this was proven by the high-intensity peak of the H_2 signal at 550 °C. A small spike in the signal at the beginning refers to the reaction that occurs at the surface of the catalyst before continuing to the bulk, as mentioned before. Overall, the decomposition of methane on reduced Ni results in the formation of CO and H_2 adatoms until reduction is complete at about 650 °C (11).[47] Consecutive oxidation of CO *via* oxygen present in NiO would lead to the formation of CO_2. However, CO oxidation is not a dominant reaction and only appears at 550 °C, as indicated by the presence of a spike in the CO_2 signal.

The results obtained from CH_4 & CO_2 conversion and H_2 & CO selectivity (Fig. 7a and b) were clear evidence of the effect of H_2 reduction on the catalyst. Inside into the reaction, H_2 reduction caused decomposition of the dolomite support which produced $Ca(OH)_2$, MgO and CaO. CH_4 was dissociated to produce carbon adatoms and H_2 and then utilized during NiO reduction. This proves that the CH_4 conversion of NiO/dolomite is much higher than Ni/dolomite. Yet, CO_2 conversion of NiO/dolomite is slightly less than Ni/dolomite. This can be correlated with the CO_2 that was produced as a side product during decomposition of dolomite from $CaCO_3$, which has an effect on the CO_2 conversion measurement. H_2 selectivity was slightly lower at the beginning of the reaction on NiO/dolomite catalyst due to the utilization of H_2 to reduce NiO to Ni^0. Meanwhile, for CO selectivity, production and oxidation of CO occurred simultaneously on NiO/dolomite caused the plot is slightly dropped. Oxidation of CO leads to the reduction of NiO to Ni^0.

3.5.2 Effect of nickel loading. The catalytic performance for various amounts of Ni loaded into the dolomite was evaluated. Based on the results obtained (Fig. 8a), 10% NiO/dolomite presented a higher percentage of CH_4 conversion (average of 98%), followed by 15% NiO/dolomite with an average of 50% CH_4 conversion. The drop in CH_4 conversion might be due to the limited accessibility of the gas reactants (CH_4 and CO_2) to

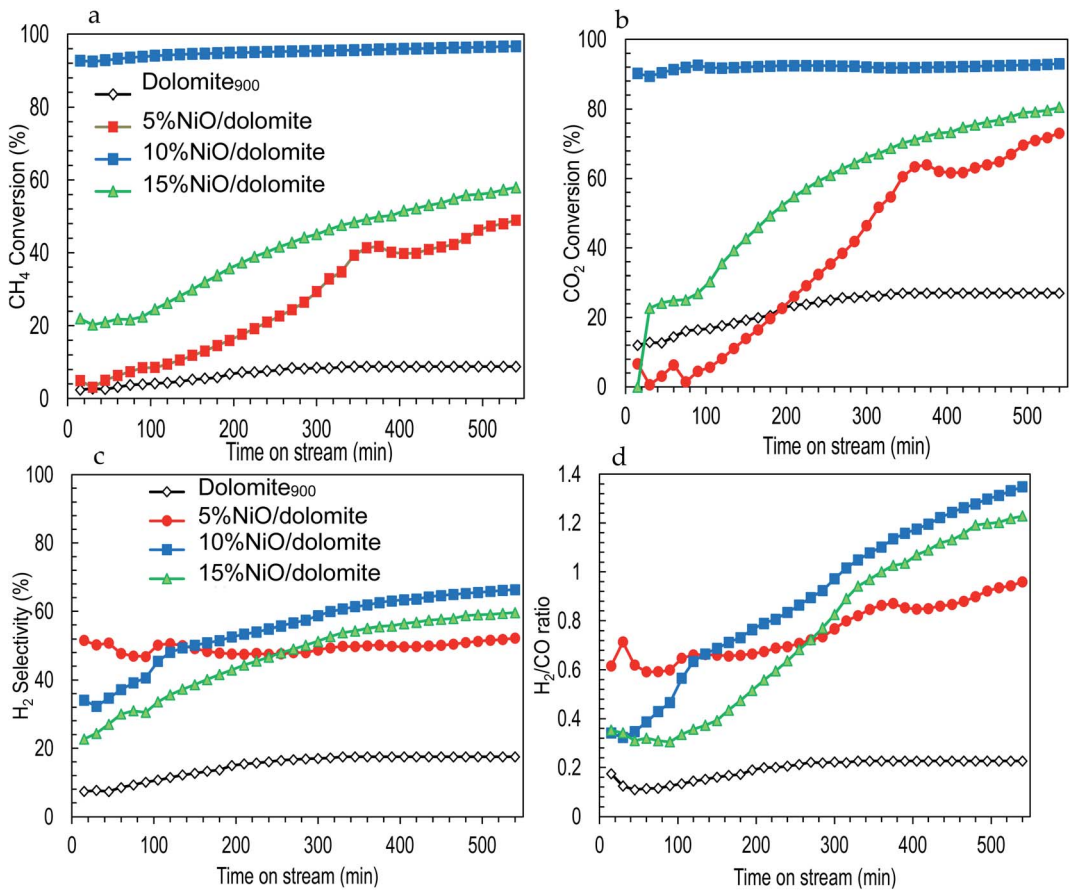

Fig. 8 Effect of nickel loading on catalytic performance of catalysts (a) CH_4 conversion (b) CO_2 conversion (c) H_2 selectivity (d) H_2/CO ratio.

the catalyst because of the low surface area and agglomeration of Ni particles (refer to Table 2). This might be affecting the active sites on the Ni catalyst which cannot react optimally for CH_4 conversion.

Fig. 8b shows CO_2 conversion which is directly proportional to the time in the stream of the DRM reaction. For the first 300 min, 10% NiO/dolomite shows higher conversion of CO_2 (up to 95%) followed by NiO. Besides, as the time increased, 15% NiO/dolomite increased rapidly up to 80% conversion. In agreement with other researchers,[7,11,13] NiO catalyst always is a good choice for the DRM reaction. Unfortunately, as time increased, the catalytic performance of Ni catalyst decreased (deactivation of the active sites) due to sintering or/and carbon deposition. In contrast, using dolomite as a support increased the catalytic performance of the Ni catalyst. However, poor textural properties (5% NiO/dolomite) and agglomeration of Ni particles (15% NiO/dolomite) lowering the catalytic activity. Meanwhile, higher temperatures and a large amount of hydrogen was consumed caused 5% NiO/dolomite to be less reactive at the beginning of the reaction, but it increased as the time of reaction increased. Dolomite showed the lowest catalytic activities, which were less than 20% CO_2 conversion due to the high attraction of Ca–Mg in dolomite to CO_2 molecules and more energy was needed to break the bond.

The H_2 production and H_2/CO ratio are displayed in Fig. 8c and d. The plotted results exhibited the same pattern of H_2 selectivity and H_2/CO ratio. The H_2 selectivity and H_2/CO ratio was in the following order: 10% NiO/dolomite > 15% NiO/dolomite > 5% NiO/dolomite > dolomite. However, in the first 3 h reaction, 5% NiO/dolomite showed remarkable H_2 selectivity and H_2/CO ratio.

It has been agreed that the dissociation of CH_4 (8) might have occurred at the beginning of reaction followed by NiO reduction to Ni^0 (9). Based on CH_4 conversion and H_2 production, these reactions tend to follow eqn (8) and (9) due to the higher conversion of CH_4 but the slightly low production of H_2 for the first 3 h of the reactions. Meanwhile, during CO_2 conversion, the strong base sites from the alkaline earth metal oxide (dolomite) tend to attract CO_2 for the formation of 'bent' $CO_2^{\partial+}$ configurations. However, the formation of these $CO_2^{\partial+}$ species alone does not lead to CO_2 activation. Therefore, surface transitions of sp metals (in this case C adatom from CH_4 dissociation), can activate CO_2 and generate CO through splitting of CO_2 by decreasing its work function.[48] Yet, the water-gas shift reaction (12), in which CO reacts with H_2O to form CO_2 and H_2, and the Boudouard reaction (3) take place for most of the catalysts, except 10% NiO/dolomite which resulted in a decrease of CO_2 conversion. Another parallel reaction involved was the reduction of CO by H_2 (ref. 48) as in the following eqn (13).

$$H_2O + CO \rightleftharpoons CO_2 + H_2 \quad (12)$$

$$CO + H_2 \rightleftharpoons C + H_2O \quad (13)$$

In general, NiO promotes acidic sites in the catalyst system. However, increasing to a high concentration of Ni metal (15% NiO) resulted in a low conversion of CH_4 and CO_2. This indicates that the parallel reactions occurred more efficiently. Hence, the products are farther from the stoichiometric proportions. This might be due to the formation of bigger crystallite sizes of NiO (less dispersed) and low quantity of Lewis acid sites. This active site is important in assisted and enhancing catalytic activities, low carbon deposition, and stable catalysts.

Another crucial piece of evidence in the catalyst life cycle is the thermal stability of the support (NiO/dolomite has high thermal stability).[49] Hence, the catalytic performance of NiO/dolomite catalysts shows a significant conversion of CH_4 and CO_2 for more than 600 minutes on stream. Therefore, using dolomites as a support will highly disperse NiO particles on the catalyst and enhance its acid–base properties.

3.5.3 Effect of reaction temperature. As shown in Fig. 9, the effect of reaction temperature on the DRM reaction is in the following order: 750 °C < 800 °C to 950 °C. The conversion of CH_4 in the first 3 h of reaction might be due to the formation of the active Ni phase at the temperature around 450 °C, which helps to dissociate CH_4 to H_2. However, by 6 to 9 h of reaction, this active phase is deactivated by coke formation, which lowers the CH_4 formation and at the same time reduces the production of H_2. For CO_2 conversion, TPD-CO_2 demonstrates an extremely high CO_2 desorption temperature (T_{max} > 750 °C) which proves a strong interaction of CO_2 with the dolomite surface. Dolomite supports adsorbing CO_2 and forms a strong bond between catalyst and reactant. High energy is required to overcome this intermolecular bonding. Consequently, CO_2 conversion becomes much lower, and CO formation is less than other reaction temperature. The strong interaction between reactant and catalyst might be a key point, but the conversion of CH_4 and CO_2 is still low. Moreover, by referring to the thermodynamic calculation of the DRM reaction as expressed by eqn (1), it only starts at a temperature of around 650 °C.[8]

Thus, as the temperature of reaction increased from 800 to 950 °C, the formation of the Ni^0 active phase increased. This propels CH_4 decomposition and enhances H_2 production. The changes in temperature also boost CO_2 conversion by intensifying carbon formation to reverse the Boudouard reaction and break down CO_2-dolomite bonding. Therefore, high and stable conversion of CH_4 and CO_2 together with H_2 selectivity can be observed for the whole reaction.

However, at 950 °C, there is a significant drop in terms of H_2 selectivity and H_2/CO ratio which is due to parallel reactions occurring. Higher temperatures and concentrations of H_2 and CO_2 inside the reactor bed enhanced reversing the WGS reaction (10) and lowering H_2 selectivity and H_2/CO ratio. Furthermore, extremely high reaction temperatures promote Ni sintering, which reduces the activity of the catalyst.

Based on the H_2/CO ratio, there are some unusual behaviours of the catalytic performance at 850 °C and 900 °C. This might be due to enhanced catalytic conversion of 10% NiO/dolomite together with parallel reactions involved during the reaction. The water gas shift reaction (12) and Bourdoard's reaction (3) might be occurring, which effectively leads to higher production of H_2 and CO. Simultaneously, conversion of CH_4 and CO_2 also happen with great enthusiasm, caused by the H_2/

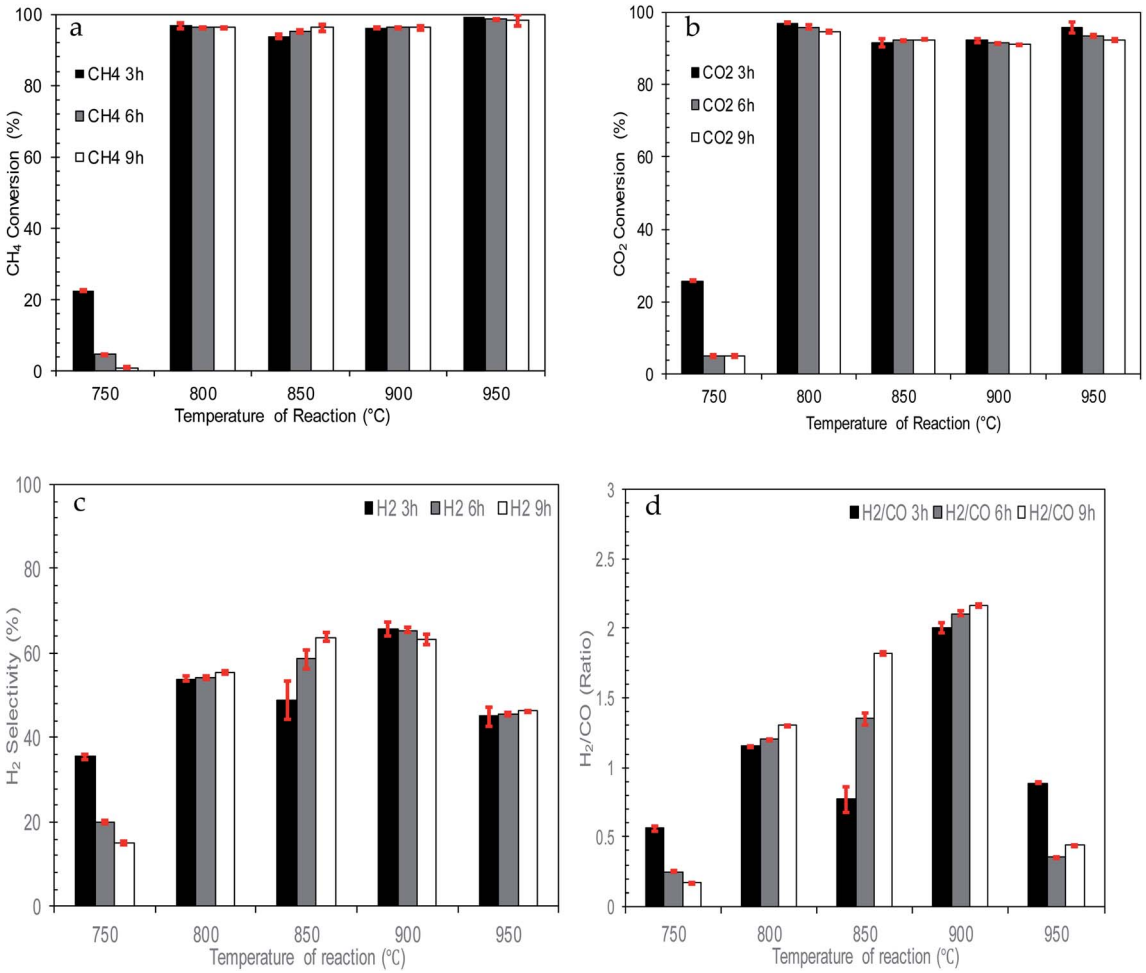

Fig. 9 Effect of reaction temperature on catalytic performance of catalysts (a) CH_4 conversion (b) CO_2 conversion (c) H_2 selectivity (d) H_2/CO ratio.

CO present at a value of more than 1. Although 850 °C and 900 °C produced higher conversion and selectivity, in terms of catalytic performance, these temperatures can disturb the reaction equilibrium, and this might have an effect in the long-term if the reaction is continued for more than 10 h.

3.6 Analysis of carbon formation on spent catalyst

Fig. 10 shows a comparison of carbon formation on fresh and spent catalysts using FESEM, TEM, XRD and TGA techniques after 10 h of DRM reaction. FESEM images of the fresh catalyst (Fig. 10a) exhibited NiO particles in aggregate form which were uniformly distributed on/in the dolomite surface by creating a solid solution and NiO particles cannot be distinguished from support. Hence, TEM images of a NiO/dolomite (Fig. 10b), and it can be confirmed that the small size of NiO particles (black) is well distributed on/into dolomite (grey) particles (fine distribution of Ni).

FESEM and TEM images of the spent catalyst after 10 h (Fig. 10c and d) show the formation of small carbon branches in between Ni and the dolomite area. This can be related to carbon growth on nickel, which is consistently distributed on dolomite. Thus, the formation of filamentous carbon (with the range of 100 to 200 nm) deposited on the surface of the catalyst is concentrated in some areas, which proves that the deposition of carbon takes place at the edges and corners of nickel species.[50,51] There are hard to be separated the carbon formation, Ni and dolomite on TEM images (Fig. 10d) due to the bulky image of NiO/dolomite during TEM analysis. The observed images can be related to the carbon-coating on the catalyst surface, because bigger and layered particles appeared. Furthermore, because of the formation of large sized carbon particles, which are nearly the same size as Ni particles, the carbon cannot be determined specifically using TEM analysis.

Fig. 10e shows XRD profiles of fresh and spent 10% NiO/dolomite catalysts run at $2\theta = 10°$ to $80°$ at the rate of $4° \text{ min}^{-1}$. The fresh catalyst only displayed two types of species (*i.e.*, dolomite and NiO) which have been discussed briefly. However, it can be observed that dolomite peaks are already diminished and replaced by three dominant phases for spent catalyst. This is due to the decomposition of dolomite under DRM reaction conditions. The most significant peaks belong to the rhombohedral $CaCO_3$ phase (ICDD 00-001-0837) at $2\theta = 23.02°$ (012), $29.36°$ (104), $36.04°$ (110), $39.49°$ (113), $43.25°$

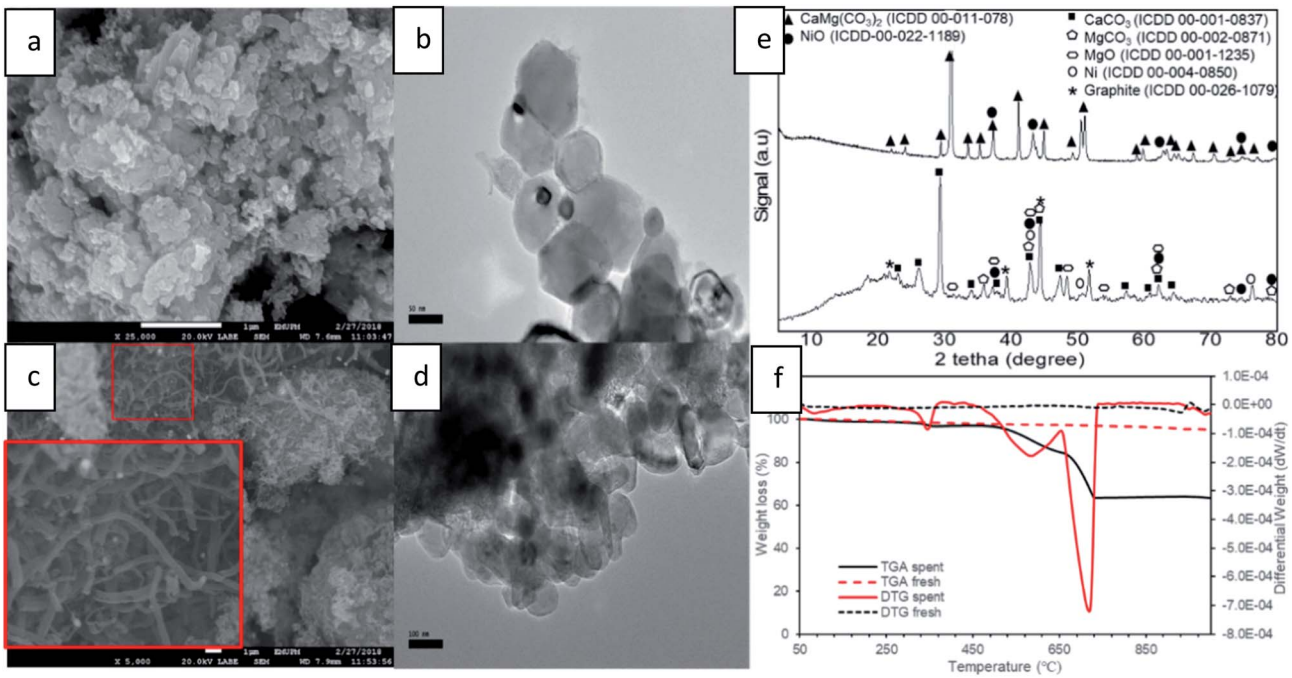

Fig. 10 Carbon formation on spent catalyst (a) FESEM fresh (b) TEM fresh (c) FESEM spent (d) TEM spent (e) XRD profiles of fresh and spent (f) TGA and DTG thermogram of fresh and spent.

(202), 47.31° (024), 48.65° (116), 57.55° (122) 62.73° (125) and 64.68° (300). Also, prominent peaks appeared that prove the existence of a $MgCO_3$ (ICDD 00-002-0871) and cubic periclase, MgO (ICDD 00-0011235). The appearance of these three peaks provide strong evidence for the decomposition of dolomite under CH_4 : CO_2 at 800 °C followed by mixed crystal formation (7). NiO species are reduced to the active phase of Ni^0 (ICDD 01-087-0712) and the existence of Ni phase at $2\theta = 44.5°$ (111), 51.85° (200) and 76.38° (220) is strong evidence that *in situ* reduction of NiO by CH_4 and/or H_2 has occurred. However, NiO species still exist after the DRM reaction, because oxidation of Ni by CO might be occurring simultaneously. Besides, the appearance of a rhombohedral graphite peak (ICCD 00-026-1079) can be correlated to the formation of filamentous carbon on FESEM and TEM.

TGA and DTG analysis (Fig. 10f) of the fresh catalyst shows very stable thermal properties because there are no peaks appearing on TGA and DTG thermograms, except for a small drop at a temperature of more than 950 °C. It might be related to the starting point of dolomite decomposition due to the extreme temperature. However, the spent catalyst shows 3-step degradation peak and the first peak of weight loss appeared at $T_{max} = 83$ °C. This prominent peak could be associated with the loss of water in the catalyst. A gradual temperature increase shows the second peak which appeared at $T_{max} = 346$ °C. This peak is due to the degradation one of the mixed crystal species. Based on the literature, $MgCO_3$, species could be degraded (1.96 wt%) around this temperature to produce MgO and CO_2.[52] Next, the obvious peak drop on both TGA and DTG thermograms is the peak recorded at $T_{max} = 580$ °C. This third weight loss was attributed to the combustion of deposited carbon material, which was about 12.26 wt% of the overall weight of catalyst during the DRM reaction. In succession, the deepest peak of degradation of other carbon material was at $T_{max} = 715$ °C. Bang *et al.* (2018) classified three different types of carbon species such as species of intermediate phase (α), encapsulated carbon (β), and filamentous carbon (γ).[53] The presence of β-type and γ-type carbon during DRM reaction is evident from FESEM and TEM analysis. Hence, the appearance of two significant peaks is associated with these types of carbon which degrade at different temperatures. Luisetto *et al.* (2015) suggested that filamentous graphitic carbon (γ) is much easier to oxidize at a lower temperature compared to deposits of graphitic carbon (β) species, due to it strongly interfered with contact between the active Ni metal and the reactant.[54] Thus, for the two peaks appearing at around 450 to 750 °C, the first peaks belong to filamentous carbon, and the second peaks belong to encapsulated/coated carbon on the surface of the catalyst.

4 Conclusions

NiO/dolomite catalysts with different NiO loadings were successfully synthesized *via* the wet impregnation method. Physicochemical properties showed that NiO/dolomite catalysts have a low surface area, but they have excellent bifunctional properties. 10% NiO/dolomite showed excellent conversion of CH_4 and CO_2 (up to 98%). This is due to its high surface area and good acid–base properties along with a lower reduction temperature. The conversions of other catalysts showed a significant increase up to 10 h on stream, and deactivation didn't occur during the reaction period. Meanwhile, 10% NiO/dolomite showed better performance on H_2 selectivity (up to

75%) and a H_2/CO ratio near to 1 : 1 and increased with increasing the time of reaction. However, using dolomite only tends to produce the lowest H_2 selectivity and H_2/CO ratio due to highly basicity properties of the catalyst. All catalysts showed H_2/CO ratio <1 at under 200 min of reaction, because the reverse water-gas shift reaction occurred to a significant extent. Other parallel reactions such as the Boudouard reaction, reduction of CO by H_2, and CH_4 decomposition might affect the conversion of CH_4 and CO_2, which is related to the production of H_2 and the H_2/CO ratio. Investigation of the reaction temperature from 750 to 950 °C revealed that too low of a temperature hindered the activity of the catalyst by lowering the formation of the Ni^0 active phase and a strong interaction between CO_2 and catalyst. Yet, too high of temperature leads to a reverse Boudouard reaction and nickel sintering, which reduces catalytic performance. Therefore, using dolomites as a support will highly disperse NiO particles on the catalyst, thus contributing to maintaining active sites and increased catalytic stability. A study of 10% NiO/dolomite spent catalyst showed that 20% carbon was deposited after 10 h reaction. The existence of the Ni and NiO phases prove that the catalyst is still stable for the DRM reaction.

Conflicts of interest

There are no conflicts to declare.

Acknowledgements

This research was funded by Kementerian Pendidikan Tinggi of Long-Term Research Grant Scheme (LRSG) NanoMITE, grant number 5526308, Putra Grant IPS, grant number 9643000 and IPM, grant number 9559000, Universiti Putra Malaysia.

References

1 O. Edenhofer, R. Pichs-Madruga, E. Y. Sokona, S. Farahani, K. Kadner, A. Seyboth, I. Adler, S. Baum, P. Brunner, B. Eickemeier, J. Kriemann, S. Savolainen, C. Schlömer, T. von Stechow and J. C. Zwickel, *IPCC, 2014: Climate Change 2014: Mitigation of Climate Change. Contribution of Working Group III to the Fifth Assessment Report of the Intergovernmental Panel on Climate Change*, 2014.
2 T. D. F. Silva and A. Costa, *Catal. Sci. Technol.*, 2013, **3**, 635–643.
3 A. M. Starik, P. S. Kuleshov, B. I. Loukhovitski and N. S. Titova, *Int. J. Hydrogen Energy*, 2015, **40**, 9872–9884.
4 J. R. H. Ross, *Catal. Today*, 2005, **100**, 151–158.
5 F. Fisher and H. Tropsch, *Brennst.-Chem.*, 1928, **9**, 39–42.
6 O. Muraza and A. Galadima, *Int. J. Energy Res.*, 2015, **39**, 1196–1216.
7 V. C. H. Kroll, H. M. Swaan and C. Mirodatos, *J. Catal.*, 1996, **161**, 409–422.
8 S. Arora and R. Prasad, *RSC Adv.*, 2016, **6**, 108668–108688.
9 J. A. Montoya, E. Romero-pascual, C. Gimon, P. Del Angel and A. Monzón, *Catal. Today*, 2000, **63**, 71–85.
10 J. Zhang and F. Li, *Appl. Catal., B*, 2015, **176–177**, 513–521.
11 S. Sokolov, E. V. Kondratenko, M. Pohl, A. Barkschat and U. Rodemerck, *Appl. Catal., B*, 2012, **113–114**, 19–30.
12 M. H. Amin, K. Mantri, J. Newnham, J. Tardio and S. K. Bhargava, *Appl. Catal., B*, 2012, **119–120**, 217–226.
13 K. Mette, S. Kühl, H. Düdder, K. Kähler, A. Tarasov, M. Muhler and M. Behrens, *ChemCatChem*, 2014, **6**, 100–104.
14 Y. Song, E. Ozdemir, S. Ramesh, A. Adishev, S. Subramanian, A. Harale, M. Albuali, B. A. Fadhel, A. Jamal, D. Moon, S. H. Choi and C. T. Yavuz, *Science*, 2020, **367**, 777–781.
15 V. R. Bach, A. C. de Camargo, T. L. de Souza, L. Cardozo-Filho and H. J. Alves, *Int. J. Hydrogen Energy*, 2020, **45**, 5252–5263.
16 Q. L. M. Ha, H. Lund, C. Kreyenschulte, S. Bartling, H. Atia, T. H. Vuong, S. Wohlrab and U. Armbruster, *ChemCatChem*, 2020, **12**, 1562–1568.
17 C. Wang, N. Sun, N. Zhao, W. Wei, Y. Sun, C. Sun, H. Liu and C. E. Snape, *Fuel*, 2015, **143**, 527–535.
18 C. Lin, J. B. Jang, L. Zhang, E. A. Stach and R. J. Gorte, *ACS Catal.*, 2018, **8**, 7679–7687.
19 P. Liang, A. Wei, Y. Liu, Y. Zhang, J. Wu, P. Liang, A. Wei, Y. Liu, Y. Zhang and J. Wu, *Mater. Res. Innovations*, 2015, **19**, 306–311.
20 Q. M. K. Waheed, C. Wu and P. T. Williams, *J. Energy Inst.*, 2015, **89**, 657–667.
21 D. Toulouse, I. M. T. M. Albi, U. M. R. Cnrs, C. Rapsodee and C. Jarlard, *Hydrogen Production From Biogas Reforming: An Overview of Steam Reforming, Dry Reforming, Dual Reforming and Tri-Reforming of Methane*, Elsevier Ltd., 2018.
22 Y. Tian, X. Zhou, S. Lin, X. Ji, J. Bai and M. Xu, *Sci. Total Environ.*, 2018, **645**, 518–523.
23 W. R. Bandi and G. Krapf, *Thermochim. Acta*, 1976, **14**, 221–243.
24 E. K. Powell and A. W. Searcy, *J. Am. Ceram. Soc.*, 1978, **61**, 216–221.
25 J. M. Valverde, A. Perejon and L. A. Perez-maqueda, *Phys. Chem. Chem. Phys.*, 2015, **17**, 30162–30176.
26 A. E. Milodowski, D. J. Morgan and S. S. J. Warne, *Thermochim. Acta*, 1989, **152**, 279–297.
27 A. H. De Aza, M. A. Rodrı, L. Rodrı, P. Convert, T. Hansen and X. Turrillas, *J. Am. Ceram. Soc.*, 2004, **85**, 881–888.
28 C. Rodriguez-Navarro, K. Kudlacz and E. Ruiz-Agudo, *Am. Mineral.*, 2012, **97**, 38–51.
29 D. F. Sibley, R. E. Dedoes and T. R. Bartlett, *Geology*, 1987, **15**, 1112–1114.
30 H. Hashimoto and T. Uematsu, *J. Solid State Chem.*, 1980, **33**, 181–188.
31 U. Kuila and M. Prasad, *Geophys. Prospect.*, 2013, **61**, 341–362.
32 J. Rouquerol, D. Avnir, C. W. Fairbridge, D. H. Everett, J. M. Haynes, N. Pernicone, J. D. F. Ramsay, K. S. W. Sing and K. K. Unger, *Pure Appl. Chem.*, 1994, **66**, 1739–1758.
33 M. Thommes, K. Kaneko, A. V. Neimark, J. P. Olivier, F. Rodriguez-reinoso, J. Rouquerol and K. S. W. Sing, *Pure Appl. Chem.*, 2015, **87**, 1051–1069.
34 M. Jullien, J. Raynal, É. Kohler and O. Bildstein, *Oil Gas Sci. Technol.*, 2005, **60**, 107–120.
35 M. Du Plessis, *Phys. Status Solidi A*, 2007, **204**, 2319–2328.

36 X. Zhong, W. Xie, N. Wang, Y. Duan, R. Shang and L. Huang, *Catalysts*, 2016, **6**, 1–12.
37 M. Varkolu, V. Velpula, D. R. Burri and S. R. R. Kamaraju, *New J. Chem.*, 2016, **40**, 3261–3267.
38 M. L. Dieuzeide, V. Iannibelli, M. Jobbagy and N. Amadeo, *Int. J. Hydrogen Energy*, 2011, **37**, 14926–14930.
39 E. Salehi, F. S. Azad, T. Harding and J. Abedi, *Fuel Process. Technol.*, 2011, **92**, 2203–2210.
40 V. R. Choudhary, A. M. Rajput and A. S. Mamman, *J. Catal.*, 1998, **585**, 576–585.
41 M. Abu Tahari, F. Salleh, S. Tengku, N. Dzakaria, A. Samsuri, M. Wahab and M. Yarmo, *Int. J. Hydrogen Energy*, 2018, **44**, 20751–20759.
42 K. V. Manukyan, A. Avetisyan, C. Shuck, S. Rouvimov, S. Kharatyan and A. S. Mukasyan, *J. Phys. Chem.*, 2015, **119**, 16131–16138.
43 R. Sokoll, H. Hobert and I. Schmuck, *J. Catal.*, 1990, **125**, 276–284.
44 A. Hakim, T. S. Marliza, N. M. A. Tahari, R. W. N. W. Isahak, R. M. Yusop, W. M. H. Mohamed and A. M. Yarmo, *Ind. Eng. Chem. Res.*, 2016, **55**, 7888–7897.
45 J. Baltrusaitis, J. Schuttlefield, E. Zeitler and V. H. Grassian, *Chem. Eng. J.*, 2011, **170**, 471–481.
46 J. Titus, M. Goepel, S. A. Schunk, N. Wilde and R. Gläser, *Catal. Commun.*, 2017, **100**, 76–80.
47 E. P. J. Mallens, J. H. B. J. Hoebink and G. B. Marin, *J. Catal.*, 1997, **167**, 43–56.
48 Y. Toda, H. Hirayama, N. Kuganathan, A. Torrisi, P. V. Sushko and H. Hosono, *Nat. Commun.*, 2013, **4**, 1–8.
49 M. M. Barroso-Quiroga and A. E. Castro-Luna, *Int. J. Hydrogen Energy*, 2010, **35**, 6052–6056.
50 H. S. Bengaard, J. K. Nørskov, J. Sehested, B. S. Clausen, L. P. Nielsen and A. M. Molenbroek, *J. Catal.*, 2002, **209**, 365–384.
51 S. Helveg, C. Lopez-Cartes, J. Sehested, P. L. Hansen, B. S. Clausen, J. R. RostrupNielsen, F. Abild-Pedersen and J. K. Nørskov, *Nature*, 2004, **427**, 5–8.
52 L. A. Hollingbery and T. R. Hull, *Thermochim. Acta*, 2010, **509**, 1–11.
53 S. Bang, E. Hong, S. W. Baek and C. Shin, *Catal. Today*, 2018, **303**, 100–105.
54 I. Luisetto, S. Tuti, C. Battocchio, S. Lo and A. Sodo, *Appl. Catal., A*, 2015, **500**, 12–22.
55 Sudarno, S. M. Razali, N. Asikin-Mijan, S. Sivasangar and Y. H. Taufiq-Yap, *Int. J. Hydrogen Energy*, 2019, **44**(37), 20738–20750.